Complete ablation of tumors using synchronous chemoradiation with bimetallic theranostic nanoparticles

Hamed Nosrati [a,b,*], Elahe Attari [a], Fatemeh Abhari [c], Murat Barsbay [d], Mohammadreza Ghaffarlou [d], Navid Mousazadeh [e], Rasoul Vaezi [f], Taras Kavetskyy [b,g,h], Hamed Rezaeejam [c], Thomas J. Webster [i], Behrooz Johari [e], Hossein Danafar [a,b,f,**]

[a] Zanjan Pharmaceutical Biotechnology Research Center, Zanjan University of Medical Sciences, Zanjan, Iran
[b] Joint Ukraine-Azerbaijan International Research and Education Center of Nanobiotechnology and Functional Nanosystems, Drohobych, Ukraine, Baku, Azerbaijan
[c] Department of Radiology, School of Paramedical Sciences, Zanjan University of Medical Sciences, Zanjan, 45139- 56184, Iran
[d] Hacettepe University, Department of Chemistry, Beytepe, Ankara, 06800, Turkey
[e] Department of Medical Biotechnology, School of Medicine, Zanjan University of Medical Sciences, Zanjan, 45139- 56184, Iran
[f] Department of Pharmaceutical Nanotechnology, School of Pharmacy, Zanjan University of Medical Sciences, Zanjan, Iran
[g] Department of Surface Engineering, The John Paul II Catholic University of Lublin, 20-950, Lublin, Poland
[h] Drohobych Ivan Franko State Pedagogical University, 82100, Drohobych, Ukraine
[i] Department of Chemical Engineering, Northeastern University, 360 Huntington Avenue, Boston, MA, 02115, United States

ARTICLE INFO

ABSTRACT

Synchronous chemotherapy and radiotherapy, termed chemoradiation therapy, is now an important standard regime for synergistic cancer treatment. For such treatment, nanoparticles can serve as improved carriers of chemotherapeutics into tumors and as better radiosensitizers for localized radiotherapy. Herein, we designed a Schottky-type theranostic heterostructure, Bi_2S_3–Au, with deep level defects (DLDs) in Bi_2S_3 as a nano-radiosensitizer and CT imaging contrast agent which can generate reactive free radicals to initiate DNA damage within tumor cells under X-ray irradiation. Methotrexate (MTX) was conjugated onto the Bi_2S_3–Au nanoparticles as a chemotherapeutic agent showing enzymatic stimuli-responsive release behavior. The designed hybrid system also contained curcumin (CUR), which cannot only serve as a nutritional supplement for chemotherapy, but also can play an important role in the radioprotection of normal cells. Impressively, this combined one-dose chemoradiation therapeutic injection of co-drug loaded bimetallic multifunctional theranostic nanoparticles with a one-time clinical X-ray irradiation, completely eradicated tumors in mice after approximately 20 days after irradiation showing extremely effective anticancer efficacy which should be further studied for numerous anti-cancer applications.

1. Introduction

Radiotherapy (RT), chemotherapy, and surgery are the most widely applied cancer treatment methods in the clinic today [1]. Drug toxicity, side effects, and nonspecific distribution are some of the limitations of chemotherapeutic drugs, such as methotrexate (MTX) [2]. The use of nanoparticles as carriers gives an opportunity to overcome these obstacles [3]. On the other hand, researchers have shown the usefulness of using natural ingredients alongside chemotherapeutic drugs for cancer

therapy [4]. Curcumin (CUR) is one of these natural products with many amazing activities used alongside chemotherapeutic drugs for diminishing their side effects and increasing therapeutic efficacy.

The therapeutic efficacy of radiotherapy is seriously afflicted by dose-limitation, also, radiation inevitably affects healthy tissues surrounding the tumor [2]. These defections cause tumors to maintain or relapse, which is rejected in cancer treatment. To protect healthy tissues surrounding the tumor from radiation hazards, radioprotective agents can be used [5,6]. CUR is one of the natural-based radioprotectors that

has recently attracted numerous researchers' attention [7–9]. Also, to enhance radiotherapy efficacy and its specificity, nanoparticles based on elements with high atomic numbers (high-Z) have been designed and used [10]. Nanoparticles with high-Z components generate secondary and auger electrons under X-ray irradiation through the photoelectric and Compton effects, leading to the production of high amounts of reactive oxygen species (ROS) within the cells [11,12].

Along these lines, bismuth sulfide (Bi_2S_3) based nanomaterials have been widely utilized in theranostic nanomedicine due to its low toxicity and exquisite features in X-ray computed tomography (CT) and near-infrared (NIR) light induced photothermal therapy (PTT) [1]. Bi_2S_3 nanomaterials, as semiconductors with a narrow band-gap energy, are capable of generating hot electrons and holes by photoexcitation [13]. These deep level defects (DLDs) in Bi_2S_3 can generate energy in terms of heat through non-radiative recombination in electrons and holes upon light irradiation based on the Shockley-Read-Hall recombination theory [14,15]. Therefore, the potential photothermal activity of Bi_2S_3 can be improved by increasing the amount of DLDs in Bi_2S_3 or by introducing more electrons to reach them.

Gold (Au) is an agent for this task. By the incorporation of Au atoms into Bi_2S_3 nanomaterials, the transfer of photoexcited electrons to the conduction band in Bi_2S_3 increases, meaning that excited electrons can non-radiatively recombine with the holes and, hence, the amount of heat released to the surrounding increases, promoting the photothermal performance of Bi_2S_3 nanoparticles [16]. This phenomenon often leads to the recombination of photogenerated electron-hole pairs, which generates low efficient free radicals in semiconductors with narrow band gaps, such as Bi_2S_3 nanoparticles [17]. The photogenerated electron-hole pairs with unique potential barriers detach efficiently when generated at the metal-semiconductor heterojunction [18,19]. Heterojunction nanomaterials composed of Au or Pd and semiconductors could enhance free radical generation *via* the Schottky barrier between them. In these types of heterojunction nanomaterials, Au or Pd components act as intrinsic radio sensitizers, in addition to their participation in the formation of Schottky heterojunctions. The combination of two nanoparticles in one platform offers some further advantages due to the integration of their individual benefits and the generation of new properties. For instance, Chang et al. synthesized a platform consisting of Au nanorods and Se nanoparticles for synergistic cancer therapy with much success [2].

Combination cancer therapy has attracted the attention of many clinicians and researchers because of its synergistic and/or additive efficacies compared to conventional mono-therapeutic techniques [20]. One of the most interesting combinations is to combine the systemic survival of chemo and spatial control of radiation therapy [21]. Numerous multifunctional nanomaterials can be combined to achieve anticancer strategies for modern enhanced cancer therapies. Using one platform of various anticancer strategy capabilities for the treatment of cancer reduces both the administration and treatment time. For example, concurrent chemoradiation therapy with Au nanoparticles and doxorubicin (DOX) loaded nanovesicles exhibited notable anticancer effects *via* a one-time injection and irradiation. Chen et al. employed high-Z mesoporous Ta_2O_5 (mTa_2O_5) nanoparticles as both a radio-sensitizer and DOX delivery system for effective chemoradiotherapy [1].

In this study, we developed a co-drug (MTX and CUR) loaded metal-semiconductor heterojunction nanoparticle as a theranostic platform for synchronous chemoradiation. Bovine serum albumin (BSA) coated Bi_2S_3 nanoparticles (Bi_2S_3@BSA) were synthesized in situ *via* the biomineralization of BSA. Bi_2S_3@BSA-Au semiconductor-metal heterojunction nanoparticles were obtained by growing Au nanoparticles on the surface of Bi_2S_3@BSA, in-situ. MTX and CUR were loaded in the Bi_2S_3@BSA-Au nanoparticles. While MTX has both a therapeutic and targeting role, CUR is involved in both radiosensitizing and radioprotection in this designed hybrid system. Using Au–Bi_2S_3 semiconductor heterojunction nanoparticles in the anti-cancer platform can enhance not only the contrast of CT images, but also free radical generation *via* the Schottky

barrier in addition to their intrinsic radiosensitizing ability.

We hypothesized here that the designed hybrid platform can simultaneously serve as a contrast agent, drug carrier, and nano-radiosensitizer in a safe and practical manner for improved cancer treatment.

2. Materials and methods

2.1. Materials

All of the materials used in this study were purchased from Sigma-Aldrich (St. Louis, USA) and Merck (Kenilworth, USA).

2.2. Methods

2.2.1. Synthesis of Bi_2S_3@BSA

Bovine serum albumin coated Bi_2S_3 (Bi_2S_3@BSA) were prepared according to processes reported earlier with a slight modification [22]. Briefly, 1.0 mL of a 50.0 mM $Bi(NO_3)_3$ solution was prepared in HNO_3. Then, under vigorous stirring, it was dumped into 8.0 mL of deionized H_2O containing 250.0 mg BSA at room temperature, and after 20 min, NaOH (1.0 M) was added drop-wise to adjust the solution pH to 12.0, and also to form a dark black suspension of Bi_2S_3@BSA. The solution was allowed to react overnight. Finally, the as-synthesized Bi_2S_3@BSA was purified by dialysis for two days and then stored at 4 °C.

2.2.2. Preparation of Bi_2S_3@BSA-Au heterojunction nanoparticles

Bi_2S_3@BSA-Au semiconductor-metal heterojunction nanoparticles were obtained *via* the growth of Au nanoparticles on the surface of Bi_2S_3@BSA, in-situ. 30.0 mg of Bi_2S_3@BSA was mixed with 304.0 μL of $HAuCl_4$ (1.0 M) and 12.0 mL of sodium citrate (1.0% w/v), followed by the drop-wise addition of fresh $NaBH_4$ (0.6 mg/mL) at room temperature (in the summer). The appearance of a cherry color confirmed the formation of Au nanoparticles on the surface of Bi_2S_3@BSA. After 12 h, dialysis was applied to purify the Bi_2S_3@BSA-Au heterojunction nanoparticles.

2.2.3. Preparation of MTX conjugated BSA (BSA-MTX)

Before adding 47.64 mg of BSA, 47.5 of mg 1-ethyl-3-(3-dimethylaminopropyl)carbodiimide (EDC), 30.0 mg of N-hydroxysuccinimide (NHS), and 23.8 mg of methotrexate sodium (MTX) were mixed in 10.0 mL of deionized H_2O and stirred for 24 h in the dark at room temperature. Then, after purification *via* dialysis, the BSA-MTX were stored at 4 °C.

2.2.4. Preparation of the Bi_2S_3@BSA-Au-BSA-MTX-CUR hybrid system

The final formulation, i.e. MTX conjugated and CUR loaded Bi_2S_3@BSA-Au nanoparticles (Bi_2S_3@BSA-Au-BSA-MTX-CUR), were obtained via a simple combination of Bi_2S_3@BSA-Au, BSA-MTX, and CUR. Briefly, before adding 26.7 mg of CUR in 1.0 mL of DMSO, 20.0 mg of Bi_2S_3@BSA-Au and 60.0 mg of BSA-MTX were mixed. The mixture was allowed to stir overnight at room temperature in order to couple each part of the hybrid system with each other. The reaction solution was centrifuged and washed with deionized water, then stored at 4 °C.

2.3. Characterization

Transmission electron microscopy (TEM, FEI 120 kV), field emission scanning electron microscopy (FESEM, FEI Quanta 200FEG) and atomic force microscopy (AFM, XE-100E PSIA) were used to identify the size and morphology of the nanoparticles. For energy dispersive X-ray (EDX) mapping, a Supra 35VP Leo EDX instrument was used. The hydrodynamic size distribution and surface charge were characterized by a Nano/zetasizer (Malvern Instruments, Nano ZS). FI-IR spectra were obtained on an infrared microscope (Bruker, Tensor 27). Thermal stability was determined by thermogravimetric analysis (TGA) (Linseis STA

PT 1000). UV–vis absorption spectra was acquired on a UV/Vis spectrophotometer (T80 double beam spectrophotometer, PG Instruments Limited). A powder X-ray diffractometer system (Malvern, PANalytical) was used for determining XRD patterns. X-ray photoelectron experiments were performed using a mono-chromatized Al K α X-ray source (Thermo Scientific).

2.4. Drug loading

MTX content of the hybrid system was determined using a dialysis bag. Briefly, 3.0 mg of the Bi_2S_3@BSA-Au-BSA-MTX-CUR and 3.0 mg of Proteinase K enzyme was added to the phosphate-buffered saline PBS containing Eppendorf tubes. After 24 h of incubation at 37 °C, the Eppendorf tube was centrifuged, then the absorbance of the supernatant at 304 nm was recorded, which related to the liberated MTX. The CUR content of the hybrid system was determined using a previous method: 3.0 mg of Bi_2S_3@BSA-Au-BSA-MTX-CUR was added to the 2.0 mL of acetone containing Eppendorf tube. The Eppendorf tube was shaken for 24 h at 37 °C, then centrifuged. The amount of desorbed CUR was calculated using the absorbance of the supernatant at 428 nm.

2.5. Drug release study

The release of MTX was performed in two conditions: in the presence and absence of a Proteinase K enzyme. To this end, 3.0 mg of Bi_2S_3@BSA-Au-BSA-MTX-CUR was dispersed in 2.0 mL of PBS containing the Proteinase K enzyme (3.0 mg, 20.0 mg/mL) and were poured into a dialysis bag, and subsequently, immersed in 30.0 mL of a PBS containing container. The container was shaken at 37 °C and 2.0 mL of an aliquot was taken from the solution at different time intervals and replaced with PBS. Then, the absorbance of the removed solution was read at 304 nm. The same protocol was applied without the Proteinase K enzyme to compare with the enzyme aided release. To appraise the CUR release profile, the same procedure was carried out in PBS containing 1.0% (v/v) tween 80. The UV–Vis absorbance of CUR was read at 428 nm. All of the procedures were performed in dark conditions.

2.6. Stability tests

The nanoparticle suspensions were prepared in different media, such as deionized water, PBS, RPMI-1640 and RPMI-1640 with 10% fetal bovine serum (FBS), then the change in the absorbance and particle size was monitored on a UV–Vis spectrophotometer and Nano-ZS instrument, respectively, at different time intervals.

2.7. In vitro studies

2.7.1. Hemocompatibility
The hemolytic activity assay was used to evaluate the hemocompatibility according to a previously reported protocol [23].

Briefly, the human red blood cell (HRBCs) solution was mixed with 0.5 mL of deionized water (positive control), 0.5 mL of PBS (negative control) and 0.5 mL of other sample suspensions at a concentration of 500 μg ml^{-1}. After shaking at 37 °C for 4 h, the eppendorf tubes were centrifuged at 13000 rpm for 15 min. Finally, the supernatant absorbance was measured by an Eppendorf Bio Photometer at λ = 540 nm. The percentage hemolysis was calculated using the following formula:

$$Hemolysis\ (\%) = \frac{A_{sample} - A_{negative}}{A_{positive} - A_{negative}} \times 100$$

2.7.2. Cell culture
A murine mammary carcinoma cell line, 4T1, and human embryonic kidney 293 cells, HEK 293, were purchased from the Pasteur Institute of Iran. The cells were cultured in the RPMI-1640 medium along with 10% fetal bovine serum, 100 units/mL of penicillin, and 50 units/mL of

streptomycin at 37 °C in an incubator at 95% relative humidity and 5% CO_2.

2.7.3. MTT assay
The MTT assay was used to measure the viability of the cells with and without X-ray irradiation. Briefly, in the MTT assay, after the programmed treating of cells, and also after passing of a proper incubation time, the MTT solution at a concentration of 3 mg/mL was added to each well, and incubated for 4h. Next, to dissolve the formed crystalline formazan dye, 150 μL of DMSO was added to the wells. Finally, the related absorbance of each well was recorded on a micro plate reader. MTT assays were carried out with 5 repetition each experiment.

2.7.4. Toxicity on healthy cells
The HEK 293 cells at a density of 7000 per well were seeded in a 96 well microplate overnight and treated with various concentrations of nanoparticles for 4 h. Then, the viability of the cells was determined with MTT assays.

Then, the treated cells were incubated overnight before measuring the viability of the cells in each well by the MTT assay.

Furthermore, the cytotoxicity of Bi_2S_3@BSA-Au was evaluated after 24 and 48 h of incubation.

2.7.5. Cellular uptake
Firstly, the nanoparticles were stained with FITC. FITC was dissolved in ethanol, and next, it was mixed for 24 h in the dark with a nanoparticle suspension at a ratio of 1:10. To purify the FITC marked nanoparticles, the reaction medium was dialyzed with deionized water in the dark. To determine the cellular uptake rate of the nanoparticles, 4T1 cells were cultured in a 24 well plate for 24 h, and next they were incubated for 4 h with FITC marked nanoparticles (Bi_2S_3@BSA 25 μg mL^{-1}). Before scanning by flow cytometry (BD Biosciences, San Jose, CA), the cells were washed with PBS.

2.7.6. In vitro chemoradiotherapy
Pre-seeded 4T1 cells in 96 well microplates at a density of 7000 per well were incubated with different nanoparticles at different concentrations for 4h. After washing the cells with PBS, they were either irradiated with an X-ray (4 Gy, during 2.10 min) or not. Then, the treated cells were incubated further for 12 h before measuring the viability of the cells in each well by the MTT assay.

2.7.7. In vitro wound healing assay
Pre-seeded 4T1 cells in 12 well plates at a density of 5×10^4 per well were scratched using the tip of a 10 μL micropipette tip (time 0 h). After incubation with different nanoparticles (25 μg mL^{-1} of a Bi_2S_3@BSA equivalent and an equivalent amount of drugs) for 4 h and also washing the cells with PBS, they were either irradiated with an X-ray (4 Gy, during 2.10 min) or not. A Nikon Microscope (ECLIPSE TS2, Tokyo, Japan) was used to capture the images during cell migration, and also ImageJ software was used to quantify the migration rate of the cells. The experiments were performed in triplicate.

2.7.8. Comet assay
A single cell gel electrophoresis test was used to evaluate DNA damage induced by the as-synthesized hybrids under X-ray irradiation. Briefly, the 4T1 cells were cultured in a 6-well plate and incubated for two days. The cells were treated with the various treatments (PBS, MTX + CUR, Bi_2S_3@BSA, Bi_2S_3@BSA-Au, Bi_2S_3@BSA-Au-BSA-MTX or Bi_2S_3@BSA-Au-BSA-MTX-CUR (Bi_2S_3@BSA 25 μg mL^{-1} and an equivalent amount of drugs)). After incubation for 4h, the culture medium of all the wells was removed and after washing with PBS was replaced with fresh culture medium. There were two plates. One of them was irradiated by an X-ray at a dose of 4 Gy (during 2.10 min) and one of them was not irradiated. After incubation for a further 12 h, the cells were harvested and then washed with PBS and subsequently re-suspended in PBS.

The microscope slides were solidified and covered with agarose, then 20 μL of re-suspended cells and 20 μL of a pre-warmed 2.0% low melting point agarose were mixed and loaded onto each slide. The slides before incubation in an alkaline electrophoresis buffer (1 mM EDTA, 300 mM NaOH) for 30 min, were immersed in a lysis buffer for 1 h. Subsequently, after neutralizing with PBS, the slides were electrophoresed at 20 V for 40 min. Next, the slides were rinsed twice in Tris-HCl buffer (0.4 mM, pH 7.5), and were stained with ethidium bromide. The DNA damage was observed under a fluorescence microscope (Olympus, Japan) and was analyzed by comet score software.

2.7.9. Imaging study

For assessing the *in vitro* CT images, the CT signal intensities in the region of interest (ROI) of different concentrations of Bi$_2$S$_3$@BSA-Au-BSA-MTX-CUR at a range of 0.0625, 0.125, 0.25, 0.5, and 1 mg/mL were measured by a CT imaging system. CT imaging parameters were as follows: full angle, averaging 3 frames, a 53 mA tube current, and a 120 kV tube voltage.

2.8. In vivo studies

2.8.1. Safety study

In order to determine the *in vivo* biosafety of the final formulation, Bi$_2$S$_3$@BSA-Au-BSA-MTX-CUR, it was injected at various doses (50, 100, 200, and 400 mg/kg) into BALB/c mice (N = 4, per group), and the mortality and body weight of the injected mice were monitored for up to 30 days. Moreover, the mice were euthanized and the major organs (i.e., heart, liver, spleen and kidney) were studied using a hematoxylin and eosin (H&E) staining assay.

2.8.2. Therapeutic effects in a mouse model with 4T1 murine mammary carcinoma tumors

BALB/C mice (15 g weight) were purchased from the Baqiyatallah University of Medical Sciences (Tehran, Iran). To establish the 4T1 murine mammary carcinoma tumor bearing mice model, a number of 1 × 10^6 4T1 cells were subcutaneously injected into the right flank of BALB/C mice. When the tumor size reached 100 mm^3, the mice were divided into twelve groups (N = 7, per group), and the *in vivo* therapeutic study started. PBS, MTX + CUR, Bi$_2$S$_3$@BSA, Bi$_2$S$_3$@BSA-Au, Bi$_2$S$_3$@BSA-Au-BSA-MTX or Bi$_2$S$_3$@BSA-Au-BSA-MTX-CUR (100 μL, Bi$_2$S$_3$@BSA 25 μg mL^{-1} and an equivalent amount of drugs) were injected *via* the tail vein, then 24 h after injection, the tumors were either irradiated with X-ray irradiation at a dose of 4 Gy (during 2.10 min) or not. During treatment duration, the tumor volume and body weight were documented. The tumor volumes were calculated by the following the formula: tumor volume = width^2 × length/2. For the histopathological evaluation of the tumors, tumors were harvested from different treatment groups at the third day post first injection. Also, after 20 days, some mice from each group were sacrificed, so key organs in these mice were harvested for histopathological evaluation. The rest of the mice were used to examine their survival rate.

2.9. Imaging study

For *in vivo* CT imaging, 250 μL of a Bi$_2$S$_3$@BSA-Au-BSA-MTX-CUR containing solution were injected into the 4T1 tumor bearing mice intravenously. CT imaging was provided pre and post injection by a CT imaging system (Philips CT scanner). The CT imaging parameters were as follows: full angle, averaging 3 frames, a 53 mA tube current, and a 120 kV tube voltage.

2.10. Statistical analysis

All acquired data were expressed as the mean ± SD (standard deviation). One-way analysis of variance was conducted for multiple group comparisons using Prism software. Significant differences between the groups were indicated by * (P < 0.05), ** (P < 0.01), *** (P < 0.001), or **** (P < 0.0001).

3. Results and discussion

3.1. Preparation of the hybrid system

A simple and facile two-step process was used to prepare Bi$_2$S$_3$@BSA-Au nanoparticles. The Bi$_2$S$_3$@BSA was synthesized *via* a BSA-mediated biomineralization process in the presence of Bi(NO$_3$)$_3$ under alkaline conditions. In this process, BSA not only served as a coating agent, but also supplied the required S atoms to form Bi$_2$S$_3$. Since the Bi$_2$S$_3$ nanostructures were coated in situ with BSA, the as-prepared Bi$_2$S$_3$@BSA nanoparticles have long-term colloidal stabilities and uniform shapes and sizes. Bi$_2$S$_3$@BSA-Au was prepared by the in situ formation of Au nanoparticles on the surface of Bi$_2$S$_3$@BSA. BSA-MTX conjugation was later obtained *via* carbodiimide coupling chemistry. Finally, the Bi$_2$S$_3$@BSA-Au-BSA-MTX-CUR formulation was obtained *via* physical interactions between Bi$_2$S$_3$@BSA-Au, BSA-MTX, and CUR. The scheme showing the synthesis process and tumor ablation mechanism of Bi$_2$S$_3$@BSA-Au-BSA-MTX-CUR is presented in Fig. 1.

3.2. Characterization

Fig. 2 shows the TEM images and corresponding size distributions of Bi$_2$S$_3$@BSA, Bi$_2$S$_3$@BSA-Au, and Bi$_2$S$_3$@BSA-Au-BSA-MTX-CUR. The Bi$_2$S$_3$@BSA showed a spherical shape (Fig. 2a and b, and Fig. S1) with an average size of ~6.2 ± 1.7 nm (mean ± SD [n = 26]), while the sizes of Bi$_2$S$_3$@BSA-Au and Bi$_2$S$_3$@BSA-Au-BSA-MTX-CUR were ~7.6 ± 2.9 nm (mean ± SD [n = 49]) and ~8.5 ± 3.0 nm (mean ± SD [n = 47]), respectively. The size of the Bi$_2$S$_3$@BSA, Bi$_2$S$_3$@BSA-Au, and Bi$_2$S$_3$@BSA-Au-BSA-MTX-CUR are uniform and of spherical shape as shown in Fig. 2. The presence of Bi$_2$S$_3$ and Au components in the heterodimers were clearly disclosed by TEM images. Because the electron density of Au is higher, the Au-rich parts of the heterodimers have darker contrast compared to the Bi$_2$S$_3$ part, as seen in Fig. 2 (d, e, g, h) [16]. Fig. 2g shows that the addition of BSA-MTX induced high aggregation of the nanoparticles.

The morphology and size of the synthesized nanoparticles were also assessed by SEM analysis, as shown in Fig. 3a–d. As shown in Fig. 3, the size of the nanoparticles increased after functionalization. Also, Fig. 3e–g show the SEM images of the Bi$_2$S$_3$@BSA nanoparticles, Bi$_2$S$_3$@BSA-Au heterodimers, and drug-loaded hybrids, as well as the corresponding elemental EDS mapping. SEM images and the elemental mappings further confirmed the particle structure, BSA coating and distribution of elements. The elemental distribution EDS-mapping confirmed the presence of Bi and Au metals in the hybrids. The overlay of the EDS mapping image of Bi, S and Bi, S and Au (in order to see the distribution of the three across the atoms) is shown in Fig. S2.

In addition, the AFM data presented in Fig. S3 confirmed that the nanoparticles grew in size as new components and were added to the hybrid nanoparticle formulation, which is consistent with the results from TEM and SEM.

To gain detailed information on the chemical states and composition of Bi$_2$S$_3$@BSA nanoparticles and Bi$_2$S$_3$@BSA-Au heterostructures, XPS analysis was employed. In the survey wide-scan of Bi$_2$S$_3$@BSA (Fig. 3h), no peaks for other elements (except C, O, N, Bi and S) were detected. An additional Au peak contributed to these elements in the spectrum of Bi$_2$S$_3$@BSA-Au heterostructures. C, O, and N atoms were the predominant species in both spectra and are attributed to the BSA in the nanoparticles. C 1s, O 1s, and N 1s core-level spectra presented in Figs. S4a–c clearly confirmed the structure of BSA and are consistent with other reports [24–26]. The high-resolution C 1s scans of Bi$_2$S$_3$@BSA are decomposed into three components, which were virtually unchanged after the addition of Au to the heterodimer nanoparticle formulation. Examination of the O 1s and N 1s spectra of Bi$_2$S$_3$@BSA-Au, on the other
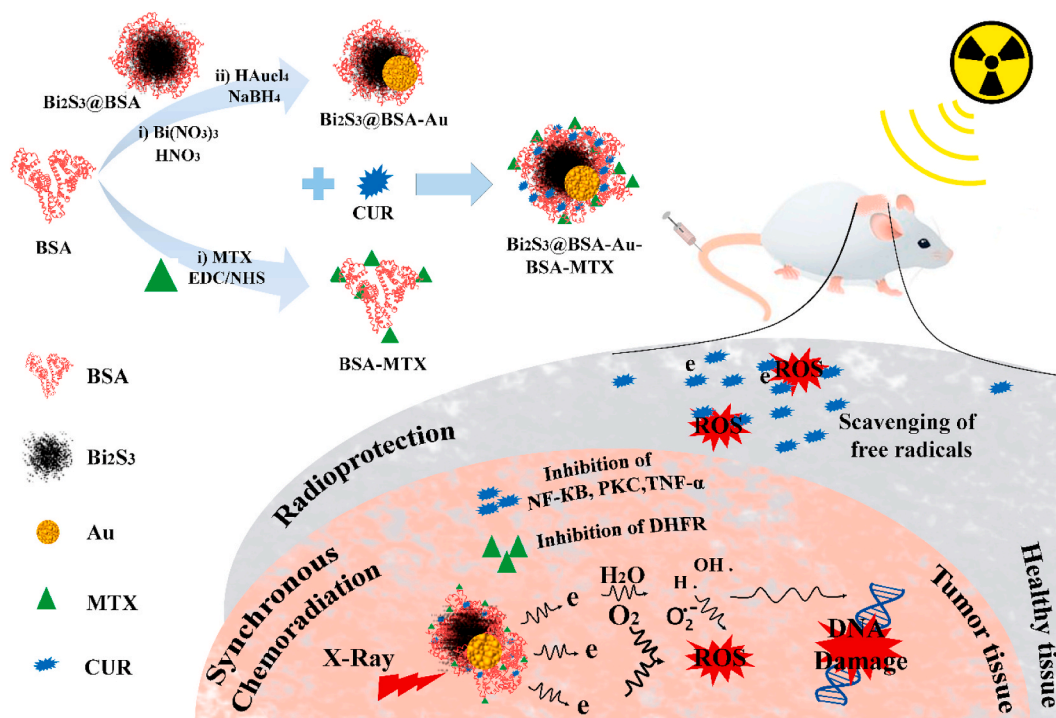
Fig. 1. The synthesis process and tumor ablation mechanism of Bi₂S₃@BSA-Au-BSA-MTX-CUR.

hand, revealed slight shifts (~0.5 eV) of O–H and –NH₂ components towards higher energies. This may be attributed to BSA's involvement in the absorption [24] and reduction [27] processes of Au(III) through –OH and –NH₂ functionalities.

The Bi 4f core-level XPS spectrum of Bi₂S₃@BSA (Fig. 3i) showed a spin–orbit doublet centered at 158.5 eV and 163.5 eV, which were assigned to Bi 4f$_{7/2}$ and Bi 4f$_{5/2}$ peaks, respectively. No peak was detected for pure Bi appearing at about a 1.0 eV higher binding energy compared to Bi₂S₃ [28]. The S 2p$_{1/2}$ component of the spin–orbit doublet of S 2p overlapped with the Bi 4f$_{5/2}$ peak of Bi₂S₃, while the S 2p$_{3/2}$ peak appeared separately at 160.5 eV. These assignments are consistent with other literature reports on Bi₂S₃ crystals [22,28,29]. As shown in Fig. 3i, the Bi 4f$_{7/2}$ peak broaden and the Bi 4f$_{5/2}$ peak could obviously decompose into two components once the Bi₂S₃–Au heterodimers formed. Chen et al. reported that the S atoms of Bi₂S₃ at the interface of the heterojunction preferred to bond to the Au atom rather than Bi as the Pauling's electronegativity of Au is larger [30]. As the incorporation of Au into Bi₂S₃ deviates S atoms from the lattice, Bi atoms occupy the S atom sites. This results in antisite Bi$_S$ (Bi replacing S) defects. Bi$_S$ antisite defects can work as DLDs [31], and therefore, improve the photothermal efficacy of Bi₂S₃ nanomaterials [30]. Antisite Bi atoms located in the defects are more electropositive compared to the lattice Bi atoms. Thus, they appeared at the higher binding energy side of the Bi 4f core-level XPS spectra. The high-resolution Au 4f XPS spectrum of the Au nanoparticles further confirmed the strong interaction between Au nanoparticles and Bi₂S₃ through the S atoms. Fig. 3j showed two peaks at 87.4 and 83.7 eV, corresponding to metallic Au 4f7/2 and 4f5/2, respectively, matching well with the literature values [19]. However, in Bi₂S₃@BSA-Au, both peaks broaden towards higher energy, meaning some Au atoms may bind to S atoms at the interface of the heterojunctions [30,32].

The average hydrodynamic diameter, related polydispersity index (PdI) and zeta potential of all the nanostructures are summarized in Fig. 4a and Fig. 4b, respectively. The hydrodynamic diameter of the final formulation, Bi₂S₃@BSA-Au-BSA-MTX-CUR, was about 152.30 ± 8.90 nm with a zeta potential of −28.50 mV. Because a large portion of designed nanostructures are composed of BSA, and could be hydrated

and swelled in aqueous environments, the hydrodynamic size of the nanoparticles was higher than their crystalline size. In addition, since BSA, Au, and Bi₂S₃ have negative surface charges, separately, the synthesized hybrid systems have high negative zeta potential, leading to high colloidal stability of the prepared nanoparticles.

Since the BSA coating of Bi₂S₃@BSA occurred in situ, the Bi₂S₃@BSA XRD pattern showed both the BSA and Bi₂S₃ peaks. As shown from the XRD pattern of Bi₂S₃@BSA in Fig. 4c, the broad peak centered at 21° was attributed to BSA [33]. Obviously, the characteristics peaks of Bi₂S₃ can also be seen in this pattern, which confirmed the successful synthesis of Bi₂S₃ via the BSA-mediated biomineralization process. The diffraction peaks located at 26.40, 29.90, 32.21, 40.60, 42.84, 46.21, and 54.12 corresponded to the (130), (211), (221), (430), (421), (431), and (351) reflections (black arrows), which matched with the standard XRD card of Bi₂S₃ (JCPDS. 17–0320) [34]. The XRD pattern of the Bi₂S₃@BSA-Au sample showed all characteristic peaks of both Bi₂S₃@BSA and Au nanoparticles. The peaks marked with star (*) in Fig. 4c at 2θ values of 38.26, 44.50, 64.89, and 77.84 corresponded to the (111), (200), (220), and (311) planes of Au nanoparticles, respectively, which matched well with the standard XRD card of Au nanoparticles (JCPDS. 89–3697) and confirmed their presence on the surface of Bi₂S₃@BSA-Au. The XRD pattern for the final formulation, Bi₂S₃@BSA-Au-BSA-MTX-CUR, verified that the crystalline structure of the nanoparticles did not changed after applying the synthesis protocol (Fig. S5). Since the samples were dispersed in PBS, additional peaks of the PBS salt were also seen in the XRD patterns.

To achieve the combined enhanced chemoradiation therapy of the two drugs, namely MTX as the chemotherapeutic and targeting agent and CUR as a natural radioprotector that improves chemotherapy and reduces side effects, they were both loaded into the nanoparticles [35, 36]. To confirm the chemical composition of the hybrid nanostructures, Uv–Vis and FTIR spectra of the samples were recorded and compared to each other. Uv–Vis spectra of BSA, MTX, BSA-MTX, and CUR are shown in Fig. S6. Fig. 4d shows the characteristic Au SPR peak at 525 nm in the UV–Vis spectra after attaching the Au nanoparticles to the surface of Bi₂S₃@BSA. Moreover, the characteristic peaks of MTX appeared at 259 nm, 307 nm, and 363 nm following the coupling of BSA and MTX. In the
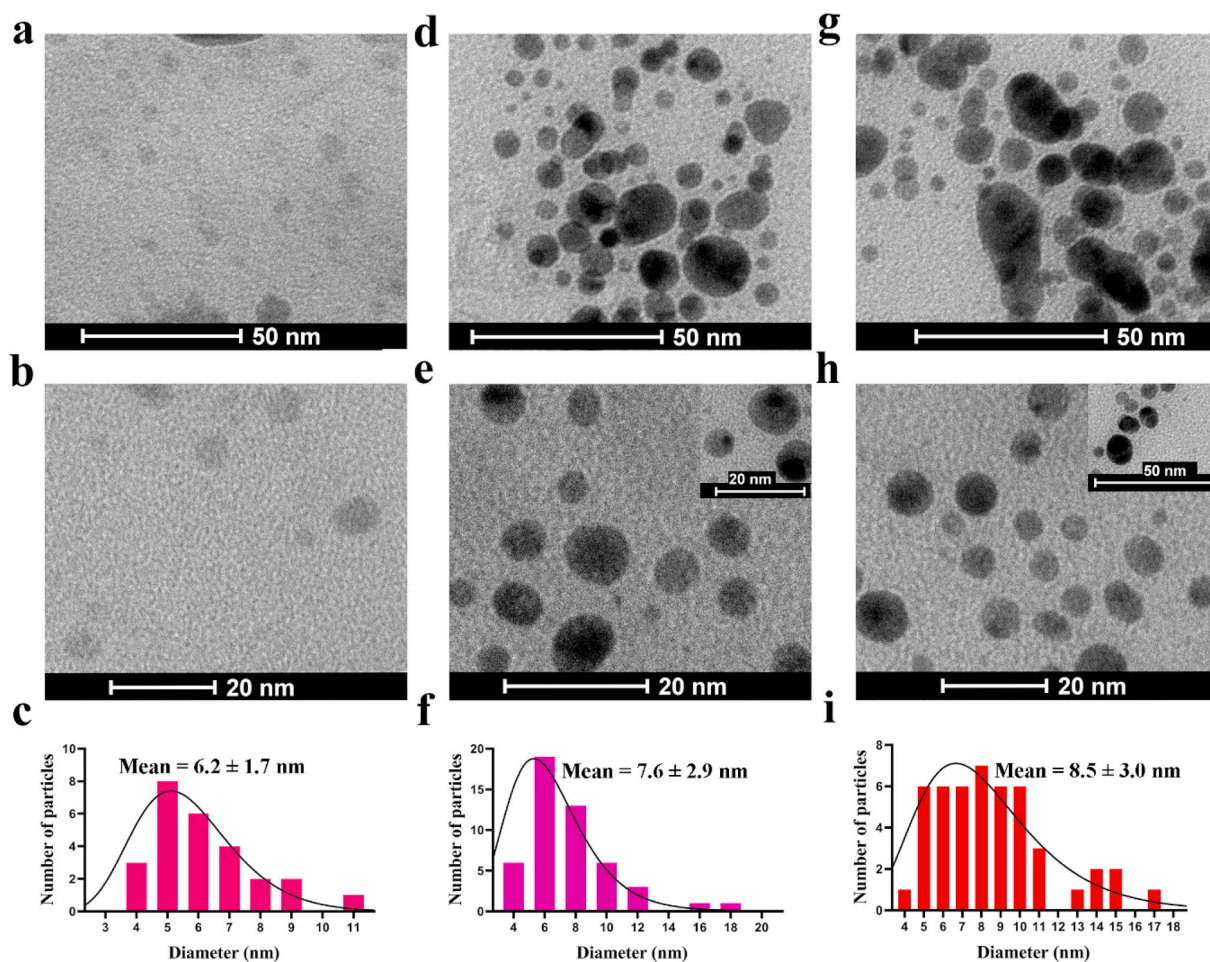
Fig. 2. Size analysis: TEM images of (a, b) Bi$_2$S$_3$@BSA; (d, e) Bi$_2$S$_3$@BSA-Au; and (g, h) Bi$_2$S$_3$@BSA-Au-BSA-MTX-CUR (the Au-rich parts of the heterodimers have darker contrast compared to the Bi$_2$S$_3$ part). Corresponding size distribution histograms of TEM images of (c) Bi$_2$S$_3$@BSA; (f) Bi$_2$S$_3$@BSA-Au; and (i) Bi$_2$S$_3$@BSA-Au-BSA-MTX-CUR (size distribution simulated using a lognormal fit).

spectrum of Bi$_2$S$_3$@BSA-Au-BSA-MTX-CUR, the characteristic absorbance bands of all the components can be seen. Compared to the other spectra, a new absorbance at 431 nm was observed, which can be attributed to CUR in the structure of the final hybrid. The interaction of CUR with BSA was investigated by Hao et al. [37]. They showed that CUR binds to BSA mainly by hydrogen bonds and van der Waals interactions and thermodynamic analysis showed that the binding process was spontaneous.

Because the large portion of the nanohybrids was composed of BSA, the FTIR spectra (Fig. 4e) of the hybrid formulations were dominated by its intense FTIR peaks. The FTIR spectra of BSA, and BSA-MTX was shown in Fig. S7a. The FTIR spectra of Bi$_2$S$_3$@BSA, Bi$_2$S$_3$@BSA-Au, Bi$_2$S$_3$@BSA-Au-BSA-MTX, and Bi$_2$S$_3$@BSA-Au-BSA-MTX-CUR obviously presented amide I and amide II bands of BSA at 1636 cm^{-1} and 1515 cm^{-1}, respectively. They also showed broad O–H and N–H stretching vibrations at 3286 cm^{-1} and 3057 cm^{-1}, respectively [38]. The new peaks appeared in the FTIR spectrum of Bi$_2$S$_3$@BSA-Au-BSA-MTX at 1077 cm^{-1} and 1204 cm^{-1} which confirmed the coupling of MTX on Bi$_2$S$_3$@BSA-Au. Similarly, the loading of CUR into the hybrid nanostructure was confirmed by the characteristic peaks of CUR in the FTIR spectrum of Bi$_2$S$_3$@BSA-Au-BSA-MTX-CUR. The expanded FTIR peaks are shown in Fig. S7b.

For anti-cancer applications, clearly, nanomaterials must be stable in physiological media. Because of their high negative surface charges, the Bi$_2$S$_3$@BSA-Au possessed excellent solubility and stability in different media, such as deionized water, PBS, RPMI-1640 and RPMI-1640 with 10% fetal bovine serum (FBS). As seen in Fig. S8, Bi$_2$S$_3$@BSA-Au

demonstrated similar absorbance and hydrodynamic sizes at different time intervals in different media. Furthermore, the absence of any precipitates in its aqueous solution after two months of storage confirmed its excellent colloidal stability.

3.3. Drug loading and releasing studies

The MTX and CUR loading amount was calculated to be 2.94 wt% and 9.15 wt%, respectively. The sustained CUR release from the Bi$_2$S$_3$@BSA-Au-BSA-MTX-CUR nanoparticles is shown in Fig. S9. In order to study the MTX release behavior, the cumulative drug release was determined in the presence and absence of proteinase K enzyme. As seen in Fig. 5a, MTX showed an enzymatic stimuli responsive release behavior. MTX release was expedited in the presence of proteinase K enzyme while its release was minimal without the enzyme. With this behavior, MTX left the nanoparticles only under harsh environments inside the lysosomes, which can then reduce off-target toxicities [39].

3.4. In vitro safety studies

3.4.1. Hemolysis assay

Assessing nanomaterial-induced hemolysis is a necessity for any blood-contacting materials. The hemolysis assay method is based on the release of hemoglobin from erythrocytes, which is measured spectrophotometrically. The hemocompatibility of the samples was appraised by a hemolysis test on HRBCs. After treatment with PBS, 500 µg/mL of Bi$_2$S$_3$@BSA, 500 µg/mL Bi$_2$S$_3$@BSA-Au, 500 µg/mL Bi$_2$S$_3$@BSA-Au-
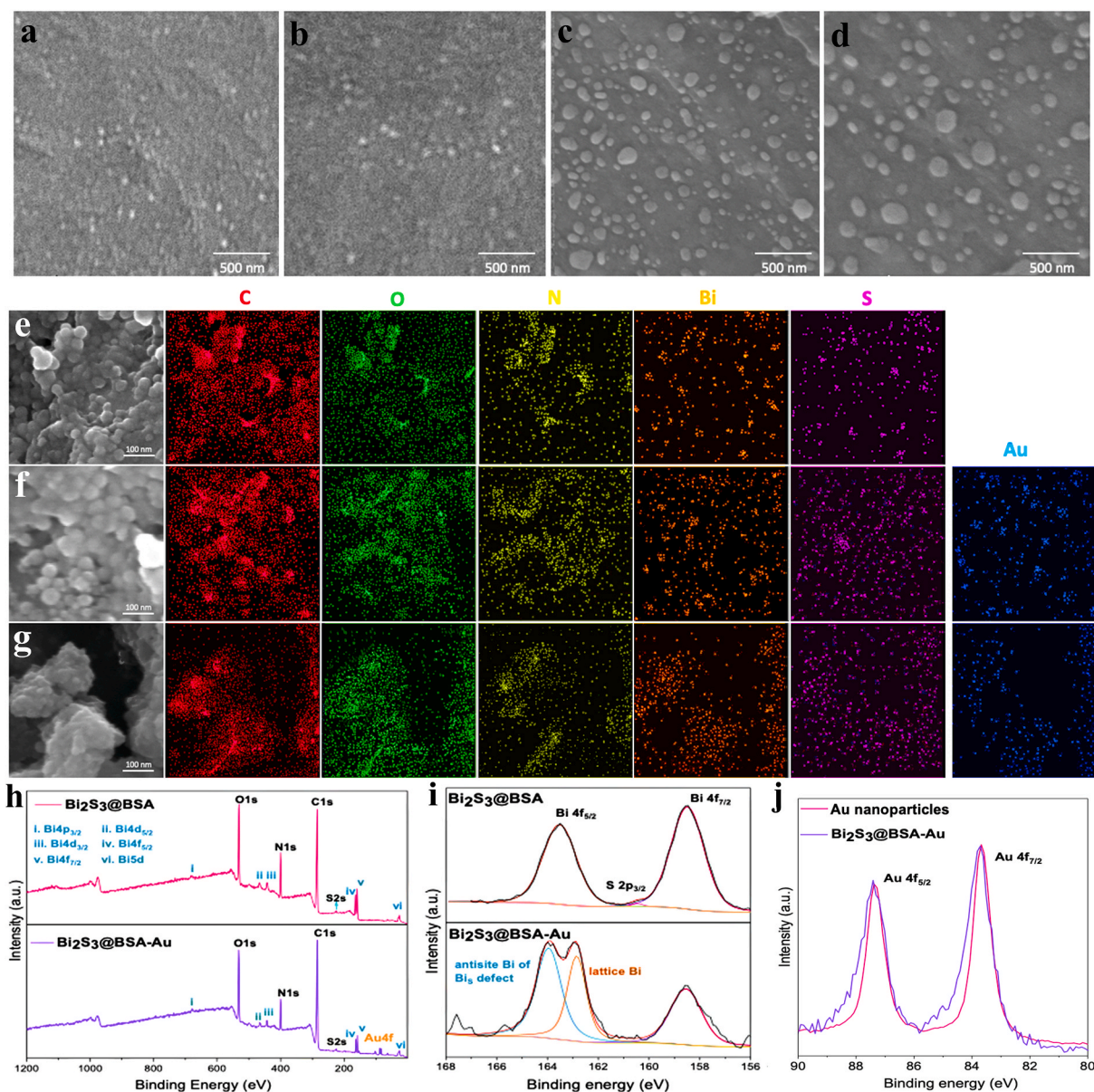
Fig. 3. Morphology and chemical composition analyses: SEM images of (a) Bi$_2$S$_3$@BSA; (b) Bi$_2$S$_3$@BSA-Au; (c) Bi$_2$S$_3$@BSA-Au-BSA-MTX; and (d) Bi$_2$S$_3$@BSA-Au-BSA-MTX-CUR. EDS elemental mapping of (e) Bi$_2$S$_3$@BSA; (f) Bi$_2$S$_3$@BSA-Au; and (g) Bi$_2$S$_3$@BSA-Au-BSA-MTX-CUR. (h) XPS survey wide scans of the Bi$_2$S$_3$@BSA nanoparticles and Bi$_2$S$_3$@BSA-Au heterodimers. (i) XPS and corresponding Gaussian fitting analysis of Bi 4f spectra and (j) Au 4f XPS spectra in Au nanoparticles and Bi$_2$S$_3$@BSA-Au.

BSA-MTX or 500 µg/mL Bi$_2$S$_3$@BSA-Au-BSA-MTX-CUR, the RBCs exhibited only a small hemolytic value (Fig. 5b), so the samples demonstrated excellent hemocompatibility.

3.4.2. Toxicity assay on healthy cells

The cytotoxicity of Bi$_2$S$_3$@BSA-Au was evaluated by MTT assays on the HEK-293 cell line. Cells treated with Bi$_2$S$_3$@BSA-Au showed good biocompatibility. As seen in Fig. 5c, the nanoparticles did not have severe cytotoxicity on healthy cells at the concentration range of 0–500 µg/mL, in that the cells showed viability higher than about 89%. Moreover, the Bi$_2$S$_3$@BSA-Au showed good biocompatibility under a long incubation time (Fig. S10).

3.5. In vitro treatment efficacy

3.5.1. Uptake efficacy

One of the concepts in the design of this study was that MTX can

serve as both a therapeutic and targeting agent. MTX not only kills cancer cells, but it can also increase the cellular uptake of nanoparticles due to its affinity towards folate receptors *via* folate receptor-mediated endocytosis [40,41]. The ability of MTX to penetrate nanoparticles into the cell was assessed on 4T1 cells by flow cytometry analysis. As shown in Fig. 5d and Fig. S11, the nanoparticles conjugated with MTX, including Bi$_2$S$_3$@BSA-Au-BSA-MTX and Bi$_2$S$_3$@BSA-Au-BSA-MTX-CUR, demonstrated higher cell uptake than Bi$_2$S$_3$@BSA-Au, which confirmed the affinity of MTX towards folate receptors.

3.5.2. MTT assay

The *in vitro* radiosensitizing ability of the synthesized nanoparticles under X-ray irradiation was examined first by an MTT assay. The concentration of Bi$_2$S$_3$@BSA, Bi$_2$S$_3$@BSA-Au, Bi$_2$S$_3$@BSA-Au-BSA-MTX, or Bi$_2$S$_3$@BSA-Au-BSA-MTX-CUR was normalized to the amount of Bi$_2$S$_3$@BSA. Also, the MTX and CUR concentrations were normalized to the equivalent amount of drugs in the nanoparticles. As can be seen in
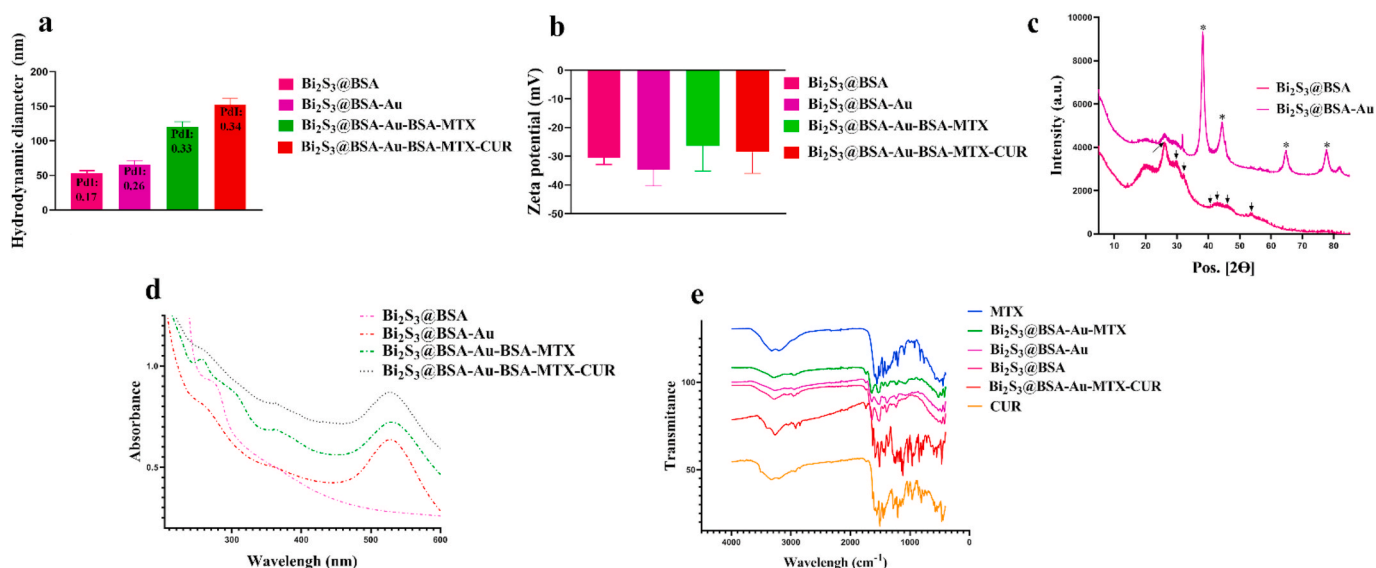
Fig. 4. Characterization: (a) Hydrodynamic size of the synthesized nanoparticles; (b) Surface charge of the synthesized nanoparticles; (c) XRD patterns of Bi_2S_3@BSA and Bi_2S_3@BSA-Au; (d) UV–Vis spectra of the samples; and (e) FTIR spectra of the samples.
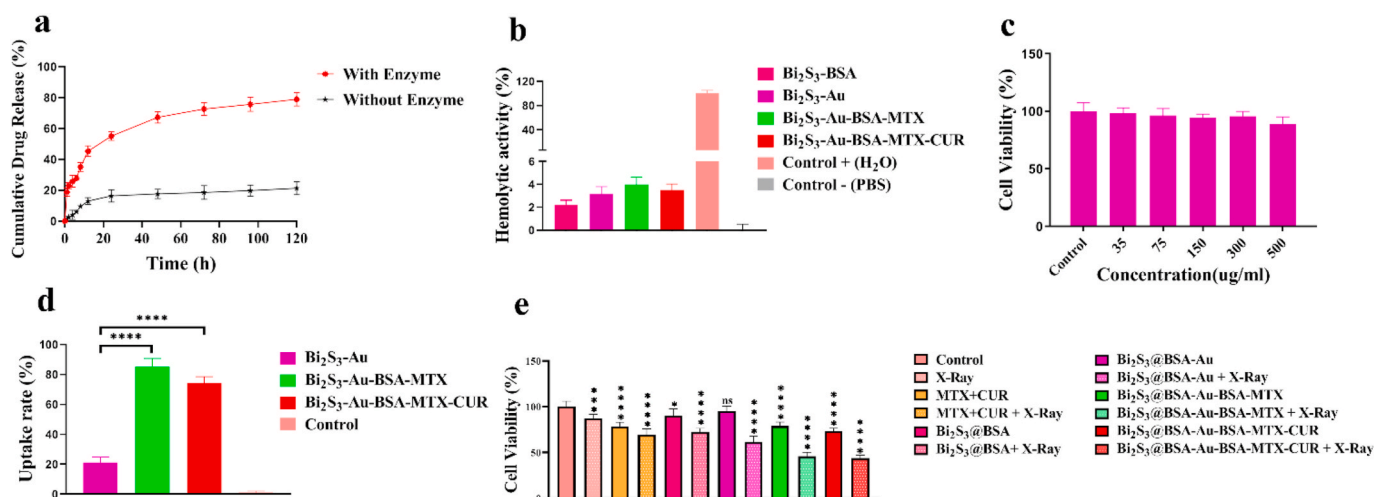
Fig. 5. In vitro assays: (a) MTX release profile in the presence and absence of the Proteinase K enzyme; (b) Hemolytic value of different formulations; (c) Cytotoxicity assay of Bi_2S_3@BSA-Au on healthy cells; (d) Cellular uptake rate of different formulations (Bi_2S_3@BSA 25 µg mL^{-1}); and (e) Cell viability test on 4T1 cells incubated with different formulations and also with and without X-ray irradiation (4Gy, during 2.10 min). Data = mean±SD; *P < 0.05, **P < 0.01, ***P < 0.001, and ****P < 0.0001 compared to the Bi_2S_3@BSA-Au-BSA-MTX-CUR + X-Ray group.

Fig. 5e, no significant cytotoxicity was detected on 4T1 cells incubated with Bi_2S_3@BSA and Bi_2S_3@BSA-Au, which is compatible with the results from the MTT assay obtained for healthy cells (Fig. 5c). Therefore, the biocompatibility of these nanoparticles was confirmed. However, the cells treated with Bi_2S_3@BSA and X-ray irradiation experienced an obvious decline in viability to 72%. Moreover, the addition of Au to the Bi_2S_3@BSA structure increased the ROS generation efficiency of the system under X-ray irradiation [16]. The cells treated with Bi_2S_3@B-SA-Au and exposed to the X-ray, showed higher toxicity, therefore, the cell viability of this group declined to 61%.

The nanoparticles functionalized with MTX showed cytotoxicity properties, which is compatible with our chemotherapy goal. The viability of 4T1 cells showed an obvious decline to 78% and 73% after treating with Bi_2S_3@BSA-Au-BSA-MTX and Bi_2S_3@BSA-Au-BSA-MTX-CUR, respectively. As seen in Fig. 5e, the cell viability of the 4T1 cells treated with both Bi_2S_3@BSA-Au-BSA-MTX and X-rays decreased further to 45%, which confirmed the ability of the combination of chemoradiation therapy of the designed nanoparticles. The therapeutic

efficacy of the designed hybrid system combining chemo and radiation therapies under X-ray irradiation was higher than the radiation or chemo therapy alone. The obtained results for the Bi_2S_3@BSA-Au-BSA-MTX-CUR + X-ray group was similar to the Bi_2S_3@BSA-Au-BSA-MTX + X-ray group, and showed higher toxicity than Bi_2S_3@BSA-Au-BSA-MTX-CUR without irradiation, which verified that the nanoparticles can trigger ROS generation within cells under X-ray irradiation.

3.5.3. Comet assay

The comet experiment (the alkaline version of the single cell gel electrophoresis assay) was carried out to confirm DNA damage by the ROS generated *via* a chemoradiation mechanism. The appearance of comet-like forms in the test results showed DNA damage, and more DNA damage results in an increase in the length of DNA migration, often referred to as the tail length (Fig. 6) [42]. The percentage DNA in the tail is another parameter indicating the extent of DNA damage (Fig. 6). Compared to the control group, cells treated with MTX + CUR experienced high DNA damage. Besides those treated with MTX + CUR and
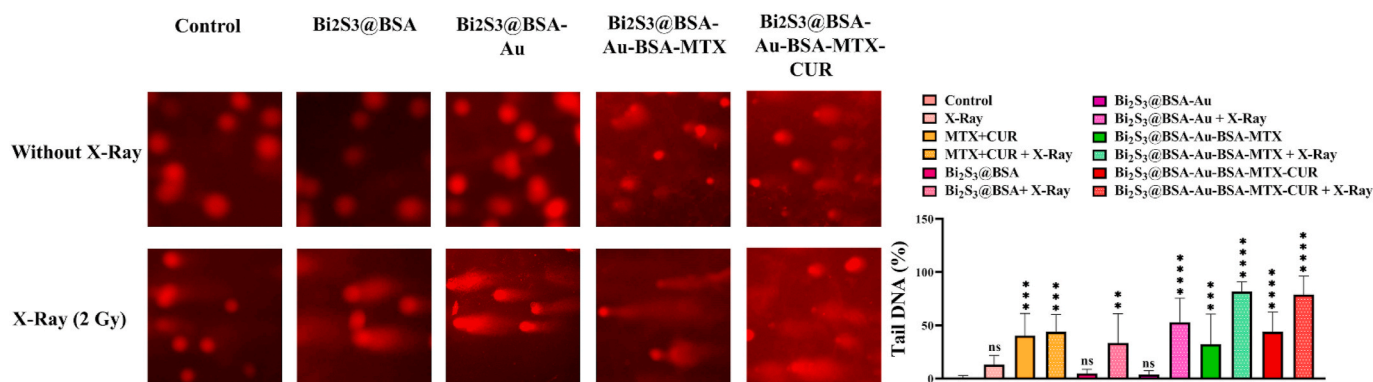
Fig. 6. Comet assay images of 4T1 cells and corresponding Tail DNA (%) after various treatment with and without X-ray irradiation (4Gy, during 2.10 min). Data = mean±SD; *P < 0.05, **P < 0.01, ***P < 0.001, and ****P < 0.0001 compared to the control group.

irradiated with X-rays showed longer tails, confirming the main goal of applying combinational chemoradiation therapy (Fig. S12). The longer comets appeared with Bi_2S_3@BSA-Au-BSA-MTX and Bi_2S_3@BSA-Au-B-SA-MTX-CUR, and much longer comets appeared under X-ray irradiation (e.g. Bi_2S_3@BSA-Au-BSA-MTX + X-Ray and Bi_2S_3@BSA-Au-BSA-MTX-CUR + X-Ray). These results obviously showed that cells treated with nanoparticles under X-ray irradiation had longer tails compared to non-irradiated groups, and thus the designed drug-loaded nanoparticles caused severe DNA damage under X-ray irradiation.

3.5.4. Wound healing assay

To further assess the ability of the designed nanoparticles in cancer therapy, cell migration was appraised by the wound healing assay. The wound healing assay area was clearly narrowed over time when cells were treated with Bi_2S_3@BSA and Bi_2S_3@BSA-Au, similar to the control group, which could confirm the non-toxicity of the carriers. The wound closure rate was lower in the groups that were treated with Bi_2S_3@BSA-Au-BSA-MTX and Bi_2S_3@BSA-Au-BSA-MTX-CUR compared to the control group. The migration inhibiting rates of Bi_2S_3@BSA-Au-BSA-MTX and Bi_2S_3@BSA-Au-BSA-MTX-CUR were 64% and 69%, respectively, while the migration inhibiting rates of Bi_2S_3@BSA and Bi_2S_3@BSA-Au were 37% and 33%, respectively. These results showed that after adding MTX and CUR on the nanoparticles, the anticancer activity of the formulations emerged. Similar results reported with the nano-diamond methotrexate prodrug showed that the migration inhibiting rate increased after MTX was added to the nano-diamond [43]. As shown in Fig. 7, the migration inhibiting rates in all groups increased under X-ray irradiation, confirming the radiosensitizing effect of Bi_2S_3 and the Au portion of the nanoparticles. Under exposure to X-rays, the migration inhibition rates of Bi_2S_3@BSA and Bi_2S_3@BSA-Au increased to 73% and 83%, respectively. The cells, when treated with

Bi_2S_3@BSA-Au-BSA-MTX and Bi_2S_3@BSA-Au-BSA-MTX-CUR and also exposed to X-rays, experienced higher migration inhibition rates of about 105% and 111%, respectively. It seems that the drug-loaded radiosensitizers not only completely inhibited the migration of the cells, but also killed some of the cells, which showed a remarkable anticancer effect for the final formulation under X-ray irradiation.

3.6. In vivo studies

Since the biocompatibility of nanomaterials is fundamental for *in vivo* applications, the *in vivo* biosafety of nanoparticles was examined in healthy mice before evaluating the antitumor effect of X-ray triggered radiosensitizers on 4T1 tumor-bearing mice. No death nor abnormal body weight changes were observed in mice injected with the nanoparticles for up to 30 days (Fig. S13). Furthermore, as shown in Fig. S14, no abnormal changes were observed in H&E stained tissues.

For tumor ablation, chemoradiation therapy with nanoparticles that function as both a drug carrier and radiosensitizer may offer some promising opportunities [21]. For the further evaluation of the ability of the designed hybrid system, *in vivo* chemoradiation therapy was conducted in a 4T1 tumor-bearing mice model. The relative tumor volume of mice treated with different treatment plans are shown in Fig. S15 and Fig. 8a. The tumor growth of the control group was rapid, similar to mice groups injected with MTX + CUR, Bi_2S_3@BSA and Bi_2S_3@BSA-Au. The tumor growth inhibition ratio of the mice groups treated with Bi_2S_3@BSA-Au-BSA-MTX and Bi_2S_3@BSA-Au-BSA-MTX-CUR was higher than the mice treated with the drug-free nanoparticles. Moreover, the tumor growth of the mice groups treated with X-ray irradiation alone and with MTX + CUR + X-ray was slightly delayed. It was shown that the mice groups treated with Bi_2S_3@BSA and Bi_2S_3@BSA-Au and irradiated with X-rays showed enhanced tumor growth inhibition, confirming their radiation sensitizing effect. Synchronous
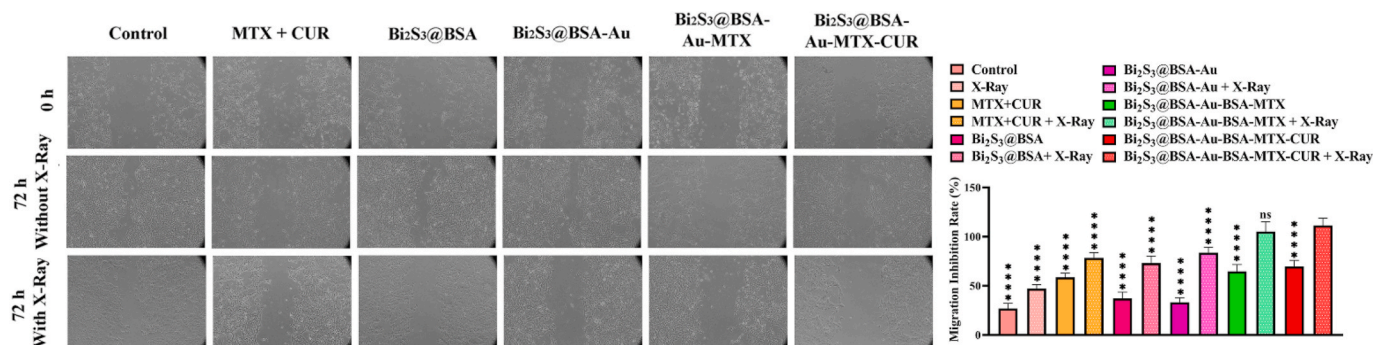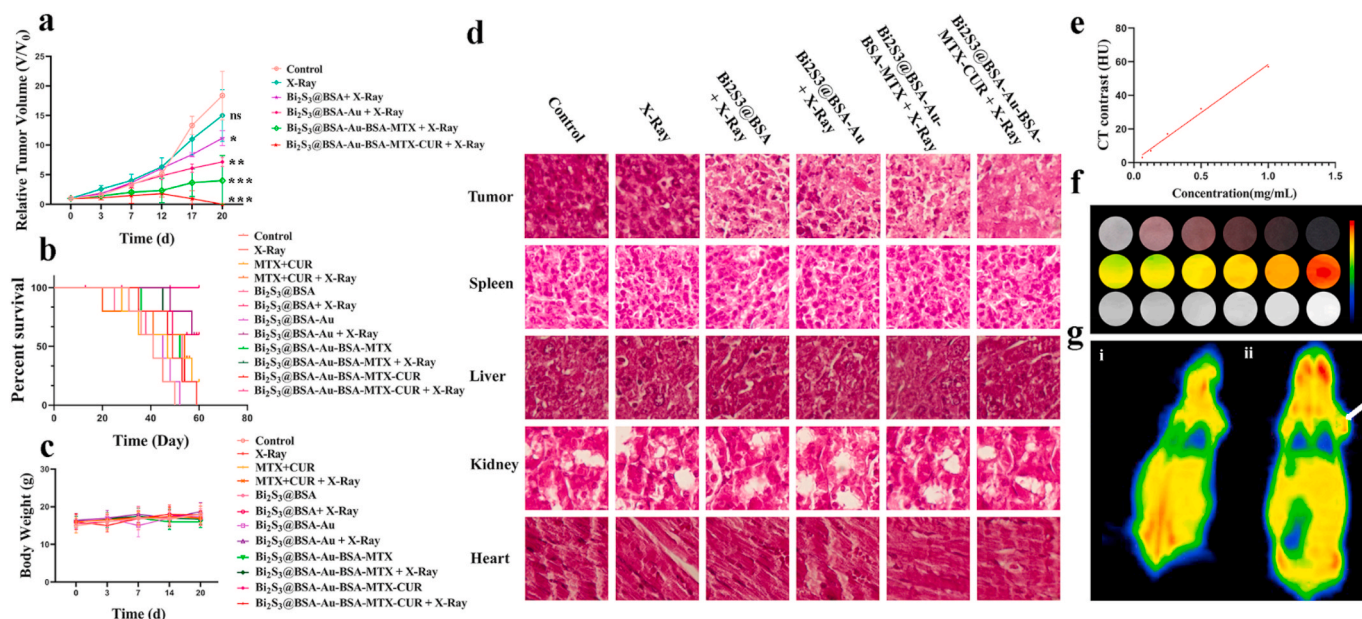

Fig. 7. Wound closure process of 4T1 cells and corresponding quantitate migration inhabitation rate (%) after various treatments with and without X-ray irradiation (4Gy, during 2.10 min). Data = mean±SD; *P < 0.05, **P < 0.01, ***P < 0.001, and ****P < 0.0001 compared to the Bi_2S_3@BSA-Au-BSA-MTX-CUR + X-Ray group.

Fig. 8. (a) Relative tumor volume, (b) Survival percentage curve, (c) body weight, and (d) histological analysis of the tumors and key organs of mice treated with different treatments; (e) X-ray attenuation of intensity in Hounsfield units (HU) of Bi_2S_3@BSA-Au-BSA-MTX-CUR at different concentrations (0.0625, 0.125, 0.25, 0.5, and 1 mg/mL); (f) First row: The typical photograph of each concentration; Second and Third rows: The CT images of each concentration; and (g) The CT images of mice with a 4T1 tumor recorded at (i) pre and (ii) post intravenous injection of Bi_2S_3@BSA-Au-BSA-MTX-CUR. Data = mean±SD; *P < 0.05, **P < 0.01, ***P < 0.001, and ****P < 0.0001 compared to the control group.

chemoradiation with both Bi_2S_3@BSA-Au-BSA-MTX and Bi_2S_3@B-SA-Au-BSA-MTX-CUR showed a superior tumor ablation effect. Remarkably, in the group of mice treated with Bi_2S_3@BSA-Au-B-SA-MTX-CUR + X-ray, not only did all of the tumors in the mice disappear without recurrence, but superiorly, no mortality was observed for up to 60 days (Fig. 8b), which may confirm the radioprotective effect of CUR. As seen in Fig. 8c, no obvious variation of body weight was observed during the treatment, which confirmed that the nanoparticles do not have clear systemic toxicity.

To further verify the therapeutic effects of the different treatment plans, H&E staining of the tumors was accomplished (Fig. 8d). For the control group, one can see deeply stained nuclei of the densely distributed cells. We can see necrotic and shadow areas in the Bi_2S_3@BSA + X-ray and Bi_2S_3@BSA-Au + X-ray groups. The H&E stained tumor results showed a higher shadow and necrotic area for both Bi_2S_3@BSA-Au-BSA-MTX + X-ray and Bi_2S_3@BSA-Au-BSA-MTX-CUR + X-ray groups. Moreover, as shown in Fig. 8d and Fig. S16, H&E staining results of key organs in the mice with various treatments indicated that there was no obvious tissue damage, proving the high biocompatibility of the nanoparticles.

3.7. Imaging studies

Bi and Au elements are mostly used as CT contrast agents due to their large X-ray attenuation coefficients (5.74 and 5.16 cm^{-2} kg^{-1} at 100 KeV). The Hounsfield unit (HU) value increased linearly by increasing the concentration of the nanoparticles (Fig. 8e). CT imaging contrast performance was seen in a series of CT images in Fig. 8f. The targeting ability and effective tumor accumulation of Bi_2S_3@BSA-Au-BSA-MTX-CUR was verified by the increase in the HU value of the tumor site in Fig. 8g. Regarding the CT contrast enhancing ability of Bi_2S_3 and Au nanoparticles, intravenous administration raised the tumor's HU value from 15 to 81 (white arrow).

4. Conclusion

In conclusion, we propose a novel multifunctional theranostic hybrid

system, Bi_2S_3@BSA-Au-BSA-MTX-CUR, consisting of Bi_2S_3–Au Schottky-type heterostructures as a nanoradiosensitizer for enhanced free radical generation and contrast agent for CT imaging, MTX as a chemotherapeutic, CUR as a nutritional supplement in chemotherapy and also radioprotector, and finally BSA as a stabilizer and to prolong blood circulation for efficient and enhanced radiochemotherapy. The modification of Bi_2S_3@BSA with Au to form Bi_2S_3@BSA-Au heterojunctions can significantly enhance free radical generation *via* the Schottky barrier. Incorporation of MTX onto Bi_2S_3@BSA-Au not only efficiently increased internalization into cancer cells to generate free radicals and secondary electron cascades under X-ray irradiation, but it can also efficiently increase cell injuries due to its inherent antitumor activity. The designed combined chemoradiation therapy plan (all in one system) showed remarkable anticancer effects, both *in vitro* and *in vivo*. Interestingly, this amazing data was achieved by a single-dose injection and one-time irradiation. A final formulation containing CUR, Bi_2S_3@BSA-Au-BSA-MTX-CUR, showed a lower Hazard Ratio than the other groups, which confirmed the radioprotection role of CUR. Moreover, *in vitro* and *in vivo* CT imaging experiments verified a promising CT contrast strength of Bi_2S_3 and Au heterojunction nanoparticles.

Ethical considerations

This study was approved by the Ethics Committee of the Zanjan University of Medical Sciences with the IR.ZUMS.REC.1397.151 ethical code, and the study participants signed an informed consent.

Data availability statement

The raw/processed data required to reproduce these findings cannot be shared at this time as the data also forms part of an ongoing study.

CRediT authorship contribution statement

Hamed Nosrati: Conceptualization, Methodology, Software, Formal analysis, Investigation, Writing – original draft. **Elahe Attari:** Investigation. **Fatemeh Abhari:** Investigation. **Murat Barsbay:** Investigation,

Software, Writing – review & editing. **Mohammadreza Ghaffarlou:** Investigation. **Navid Mousazadeh:** Investigation. **Rasoul Vaezi:** Investigation. **Taras Kavetskyy:** Investigation, Resources. **Hamed Rezaeejam:** Investigation. **Thomas J. Webster:** Writing – review & editing. **Behrooz Johari:** Investigation. **Hossein Danafar:** Funding acquisition, Writing – review & editing.

Declaration of competing interest

The authors declare that they have no known competing financial interests or personal relationships that could have appeared to influence the work reported in this paper.

Acknowledgments

Appendix A. Supplementary data

Supplementary data to this article can be found online at https://doi.org/10.1016/j.bioactmat.2021.05.015.

References

[1] Y. Chen, G. Song, Z. Dong, X. Yi, Y. Chao, C. Liang, K. Yang, L. Cheng, Z. Liu, Small 13 (2017) 1602869.
[2] Y. Chang, L. He, Z. Li, L. Zeng, Z. Song, P. Li, L. Chan, Y. You, X.-F. Yu, P.K. Chu, ACS Nano 11 (2017) 4848–4858.
[3] Z. Wang, X. Xue, Y. He, Z. Lu, B. Jia, H. Wu, Y. Yuan, Y. Huang, H. Wang, H. Lu, Adv. Funct. Mater. 28 (2018) 1802159.
[4] C. Brami, T. Bao, G. Deng, Crit. Rev. Oncol.-Hematol. 98 (2016) 325–334.
[5] H. Rezaeejam, A. Shirazi, P. Izadi, J.T. Bazzaz, M. Ghazi-Khansari, M. Valizadeh, G. A. Tabesh, J. Canc. Res. Therapeut. 14 (2018) 1070.
[6] M. Valizadeh, A. Shirazi, P. Izadi, J.T. Bazzaz, H. Rezaeejam, G.A. Tabesh, Biosci Biotechnol Res Commun 9 (2016) 821–827.
[7] S. Kolivand, P. Amini, H. Saffar, S. Rezapoor, E. Motevaseli, M. Najafi, F. Nouruzi, D. Shabeeb, A.E. Musa, Curr. Rad. 12 (2019) 23–28.
[8] H. Bagheri, S. Rezapour, M. Najafi, E. Motevaseli, B. Shekarchi, M. Cheki, H. Mozdarani, Iran. J. Med. Sci. 43 (2018) 645.
[9] M. Ahmed, M.A. Qadir, A. Hameed, M.N. Arshad, A.M. Asiri, M. Muddassar, Bioorg. Chem. 76 (2018) 218–227.
[10] Y. Zang, L. Gong, L. Mei, Z. Gu, Q. Wang, ACS Appl. Mater. Interfaces 11 (2019) 18942–18952.
[11] Q. Liu, Y. Shi, Y. Chong, C. Ge, ACS Applied Bio Materials 4 (2) (2021) 1843–1851.
[12] W. Fu, X. Zhang, L. Mei, R. Zhou, W. Yin, Q. Wang, Z. Gu, Y. Zhao, ACS Nano 14 (2020) 10001–10017.
[13] W. Pelouch, R. Ellingson, P. Powers, C. Tang, D. Szmyd, A. Nozik, Phys. Rev. B 45 (1992) 1450.
[14] X. Ji, B. Liu, Y. Xu, H. Tang, X. Li, H. Gong, B. Shen, X. Yang, P. Han, F. Yan, J. Appl. Phys. 114 (2013) 224502.
[15] M. Cappelletti, A. Cedola, E.P. y Blancá, Semicond. Sci. Technol. 24 (2009) 105023.
[16] F. Abhari, J. Charmi, H. Rezaeejam, Z. Karimimoghaddam, H. Nosrati, H. Danafar, A. Farajollahi, ACS Sustain. Chem. Eng. 8 (2020) 5260–5269.
[17] Z. Zhang, W. Wang, L. Wang, S. Sun, ACS Appl. Mater. Interfaces 4 (2012) 593–597.
[18] E. Ha, L.Y.S. Lee, J. Wang, F. Li, K.Y. Wong, S.C.E. Tsang, Adv. Mater. 26 (2014) 3496–3500.
[19] X. Wang, C. Zhang, J. Du, X. Dong, S. Jian, L. Yan, Z. Gu, Y. Zhao, ACS Nano 13 (2019) 5947–5958.
[20] D.A. Zarin, T. Tse, J. Sheehan, N. Engl. J. Med. 372 (2015) 174–180.
[21] Z. Zhou, A. Chan, Z. Wang, X. Huang, G. Yu, O. Jacobson, S. Wang, Y. Liu, L. Shan, Y. Dai, Angew. Chem. Int. Ed. 57 (2018) 8463–8467.
[22] Y. Wang, Y. Wu, Y. Liu, J. Shen, L. Lv, L. Li, L. Yang, J. Zeng, Y. Wang, L.W. Zhang, Adv. Funct. Mater. 26 (2016) 5335–5344.
[23] H. Nosrati, J. Charmi, M. Salehiabar, F. Abhari, H. Danafar, ACS Biomater. Sci. Eng. 5 (2019) 4416–4424.
[24] A. Belatik, S. Hotchandani, R. Carpentier, H.-A. Tajmir-Riahi, PloS One 7 (2012).
[25] Q. Yang, L. Wei, X. Zheng, L. Xiao, Sci. Rep. 5 (2015) 17727.
[26] M.M. Millard, M. Friedman, Biochem. Biophys. Res. Commun. 70 (1976) 445–451.
[27] I. Matei, C.M. Buta, I.M. Turcu, D. Culita, C. Munteanu, G. Ionita, Molecules 24 (2019) 3395.
[28] J. Grigas, E. Talik, V. Lazauskas, Phys. Status Solidi 232 (2002) 220–230.
[29] K. Ai, Y. Liu, J. Liu, Q. Yuan, Y. He, L. Lu, Adv. Mater. 23 (2011) 4886–4891.
[30] Y. Cheng, Y. Chang, Y. Feng, H. Jian, Z. Tang, H. Zhang, Angew. Chem. Int. Ed. 57 (2018) 246–251.
[31] D. Han, M.-H. Du, C.-M. Dai, D. Sun, S. Chen, J. Mater. Chem. 5 (2017) 6200–6210.
[32] L.A. Porter Jr., D. Ji, S.L. Westcott, M. Graupe, R.S. Czernuszewicz, N.J. Halas, T. R. Lee, Langmuir 14 (1998) 7378–7386.
[33] P. Yang, Q. Liu, J. Liu, H. Zhang, Z. Li, R. Li, L. Liu, J. Wang, Ind. Eng. Chem. Res. 56 (2017) 3588–3598.
[34] D.R. Kumar, S. Kesavan, M.L. Baynosa, J.-J. Shim, J. Colloid Interface Sci. 530 (2018) 361–371.
[35] Z. Fan, Y. Wang, S. Xiang, W. Zuo, D. Huang, B. Jiang, H. Sun, W. Yin, L. Xie, Z. Hou, J. Mater. Chem. B (2020).
[36] J. Xie, Y. Yong, X. Dong, J. Du, Z. Guo, L. Gong, S. Zhu, G. Tian, S. Yu, Z. Gu, ACS Appl. Mater. Interfaces 9 (2017) 14281–14291.
[37] C. Hao, G. Xu, T. Wang, Z. Lv, K. Zhu, B. Li, S. Chen, R. Sun, Russ. J. Phys. Chem. B 11 (2017) 140–145.
[38] J. Yan, F. Wang, J. Chen, T. Liu, T. Zhang, International Journal of Polymer Science (2016) 2016.
[39] N. Kohler, C. Sun, J. Wang, M. Zhang, Langmuir 21 (2005) 8858–8864.
[40] Y. Li, J. Lin, Z. Cai, P. Wang, Q. Luo, C. Yao, Y. Zhang, Z. Hou, J. Liu, X. Liu, J. Contr. Release 321 (2020) 222–235.
[41] Y. Zhang, Y. Li, H. Tian, Q. Zhu, F. Wang, Z. Fan, S. Zhou, X. Wang, L. Xie, Z. Hou, Mol. Pharm. 16 (2019) 3133–3144.
[42] X. Nie, L. Xia, H.-L. Wang, G. Chen, B. Wu, T.-Y. Zeng, C.-Y. Hong, L.-H. Wang, Y.-Z. You, ACS Appl. Mater. Interfaces 11 (2019) 31735–31742.
[43] W. Zhao, S. Wei, H. Zhao, Y. Li, R. Wu, J. Wang, Diam. Relat. Mater. 77 (2017) 171–180.